

Geofluid behaviour in successive extensional and compressional events: a case study from the southwestern end of the Vallès-Penedès Fault (Catalan Coastal Ranges, NE Spain)

V. Baqués*, A. Travé, E. Roca, M. Marín and I. Cantarero

Geomodels Research Institute, Faculty of Geology, University of Barcelona, c/Martí i Franquès s/n, 08028 Barcelona, Spain

*Corresponding author (e-mail: vbaques@ub.edu)

ABSTRACT: The structural position of the Upper Jurassic–Lower Cretaceous carbonates located in the central part of the Catalan Coastal Ranges corresponds to the southwestern end of the Vallès-Penedès Fault. This fault was reactivated at different times during successive extensional and compressional events and several generations of fractures and cementations were formed.

Based on petrological and geochemical analyses of this cementation an evolution of the fluids related to the different tectonic stages can be deduced. (1) During the Mesozoic extension, the parent fluids resulted either from a mixing of trapped Upper Jurassic–Lower Cretaceous seawater and meteoric water, or from buffered meteoric waters. (2) Related to the Paleogene compression, the fluids came from the percolation of meteoric waters indicating shallow-depth deformation. (3) During the transitional phase between Paleogene compression and Neogene extension, a karstic dissolution took place and the porosities were infilled by different generations of sediments and cements deposited from meteoric fluids. (4) During the Neogene extension several episodes of meteoric percolations and fracturing processes occurred. The Neogene extensional faults used the earlier karstic system to develop and, later, during the late post-rift stage, a new karstic system occurred, covering the walls of open fractures with speleothems.

INTRODUCTION

In sedimentary basins, deformation and fracturing processes influence the distribution of diagenetic episodes because they are discontinuities that can act as barriers or as conduits for fluid circulations and cause the mobilization of these fluids from reactivation in different episodes of tectonic activity (Sibson 1987; Agosta *et al.* 2007; Breesch *et al.* 2009). Knowing the distribution of fractures, it is possible to predict the potential hydrocarbon and aquifer reservoirs, as well as to assess their quality (Knipe & McCaig 1994; Labaume *et al.* 2004; Géraud *et al.* 2006; Bussolotto *et al.* 2007). The study of fracture-related carbonate precipitates, coupling microstructural, petrological and geochemical analyses, allows one to unravel the origin and pathways of the fluids (De Brit 1989; Muech *et al.* 1995; Bitzer *et al.* 1997; Travé *et al.* 1998; 2004; 2009; Travé & Calvet 2001; Labaume *et al.* 2007; Micarelli *et al.* 2005; 2006; Benedicto *et al.* 2008; Vilasi *et al.* 2009; André *et al.* 2010). In addition, specific petrophysical properties of the fractured host-rock and the pressure, temperature, origin and behaviour of fluids will control the degree of fluid–rock interaction and precipitation of cements within the fractures. However, these processes depend not only on the lithology; the depth at which the deformation develops is also one of the main factors controlling the diagenetic

behaviour of the fractured areas. For example, it is known that the development of fractures in carbonates at shallow crustal depths (<1–3 km) is a very complex process, because of the interaction of mechanical and chemical processes (Sibson 2000; Pili *et al.* 2002; Verhaert *et al.* 2009).

The present study has been focused on characterizing the evolution of fluids within a long basement-involved fault which shows a complex tectonic evolution due to the superposition of successive extensional and compressional events. The case study is the Vallès-Penedès Fault, located in the central part of the Catalan Coastal Ranges, in the northeastern part of Spain. The main aims followed are: (1) to characterize the distribution and chronology of fractures, the timing of diagenetic processes, the type of fault rocks and related cements and the fluids involved during different deformation events; (2) to characterize the differences between the Mesozoic and Neogene extensional events; and (3) to recognize the interference between karstic and tectonic processes. The interest in the study of the karst development and infilling is because the main hydrocarbon reservoirs in Spain are located offshore in the Mediterranean, in Mesozoic reservoirs, equivalent to those studied onshore. For this reason, the diagenetic study can be compared in both areas, and the studied outcrops can be used as analogues of the reservoirs present in the Valencia Trough.

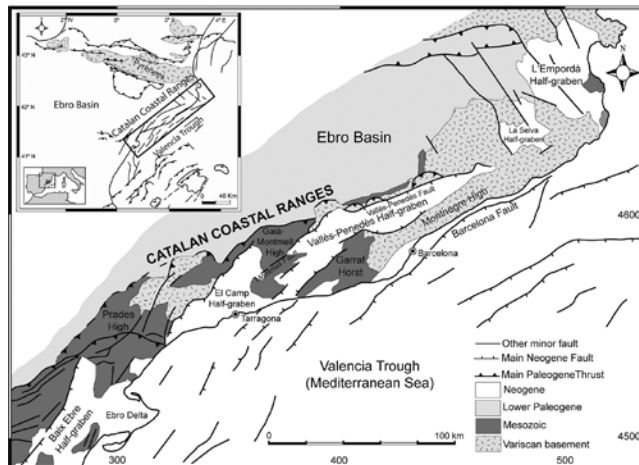


Fig. 1. Simplified geological map of the Catalan Coastal Ranges. Coordinates are in UTM (km).

GEOLOGICAL SETTING

The Catalan Coastal Ranges (CCR), in the NE of Spain, constitute the onshore expression of the northeastern part of the continental margin that separates the thinned crust of the Valencia Trough from the Iberian crust of the Iberian Plate (Dañoibeitia *et al.* 1992; Vidal *et al.* 1995). It consists of several ENE- to NE-striking blocks bounded by 50–150 km long basement-involving faults which display a right-stepping *en echelon* arrangement with an ENE–WSW strike (Fig. 1). These faults dip southeastwards and show a reverse and/or normal motion. This double motion of

the faults, together with the internal structure of the bounded blocks, reflects a complex evolution in which three main tectonic events can be differentiated: (1) a Mesozoic extensional phase in which several Late Jurassic–Early Cretaceous extensional basins developed along the present-day CCR (Montmelé-Garraf, Barcelona, El Perelló and Maestrat Basins; Salas 1987); (2) a Paleocene to middle Oligocene contractional phase that generated an intraplate chain (the Catalan Intraplate Belt) from the emplacement of ENE- to NE-trending thick-skinned thrust sheets bounded by SE-dipping thrusts with a limited left-lateral strike-slip motion (Ashauer & Teichmüller 1935; Llopis-Lladó 1947; Anadón *et al.* 1985; Guimerà 1988, 2004; Roca 1996); and (3) a late Oligocene?–Neogene extensional phase leading to the normal reactivation of some of the main Paleogene faults (Fontboté 1954; Amigo 1986; Gaspar-Escribano *et al.* 2004) which split the area in a set of ENE–WSW blocks mainly tilted toward the NW (Bartrina *et al.* 1992; Roca & Guimerà 1992).

In this regional setting, the study area is placed at the southwestern end of the main outcropping basement fault: the Vallès-Penedès Fault (Fig. 2). This fault is more than 100 km long and has a Neogene extensional displacement that reaches 4 km (Roca *et al.* 1999). It belongs to a long-lived fault that, before this extensional motion, moved as a Paleogene NW-directed thrust (Fontboté 1954) and controlled the northwestern boundary of the Late Jurassic–Early Cretaceous Garraf-Montmelé Basin (Salas 1987). The kinematics and structure of the Mesozoic history of the Vallès-Penedès Fault can be inferred from the study of the soft linkage zone that connects this fault with the other CCR major outcropping fault to the El Camp Fault (Fig. 2). This linkage zone is formed by pre-Neogene rocks and includes an ENE–WSW strip of folds and thrusts that, located at the southwestern prolongation of the Neogene Vallès-Penedès Fault, separates two realms with different Mesozoic successions. The

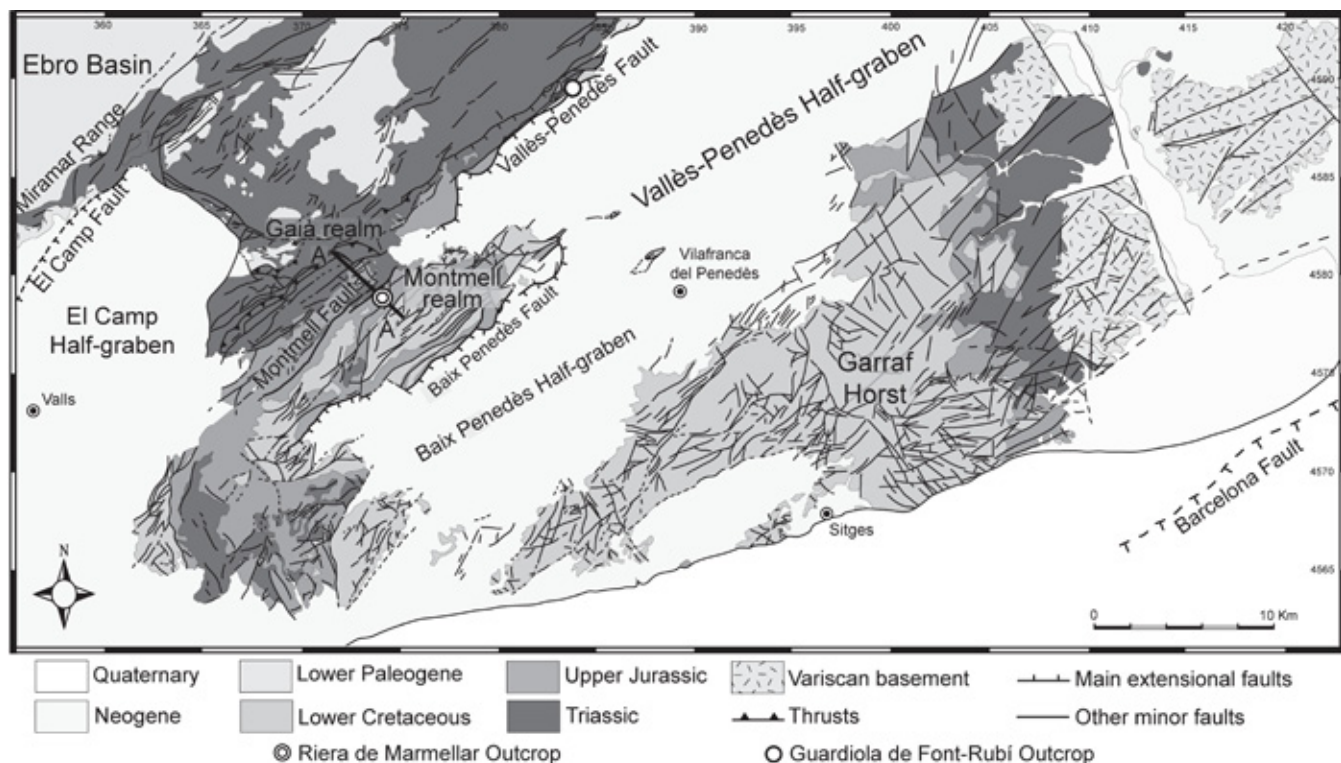


Fig. 2. Geological map of the southwestern segment of the Vallès-Penedès half-graben with location of the studied outcrops and the cross-section depicted in Figure 3. Coordinates are in UTM (km).

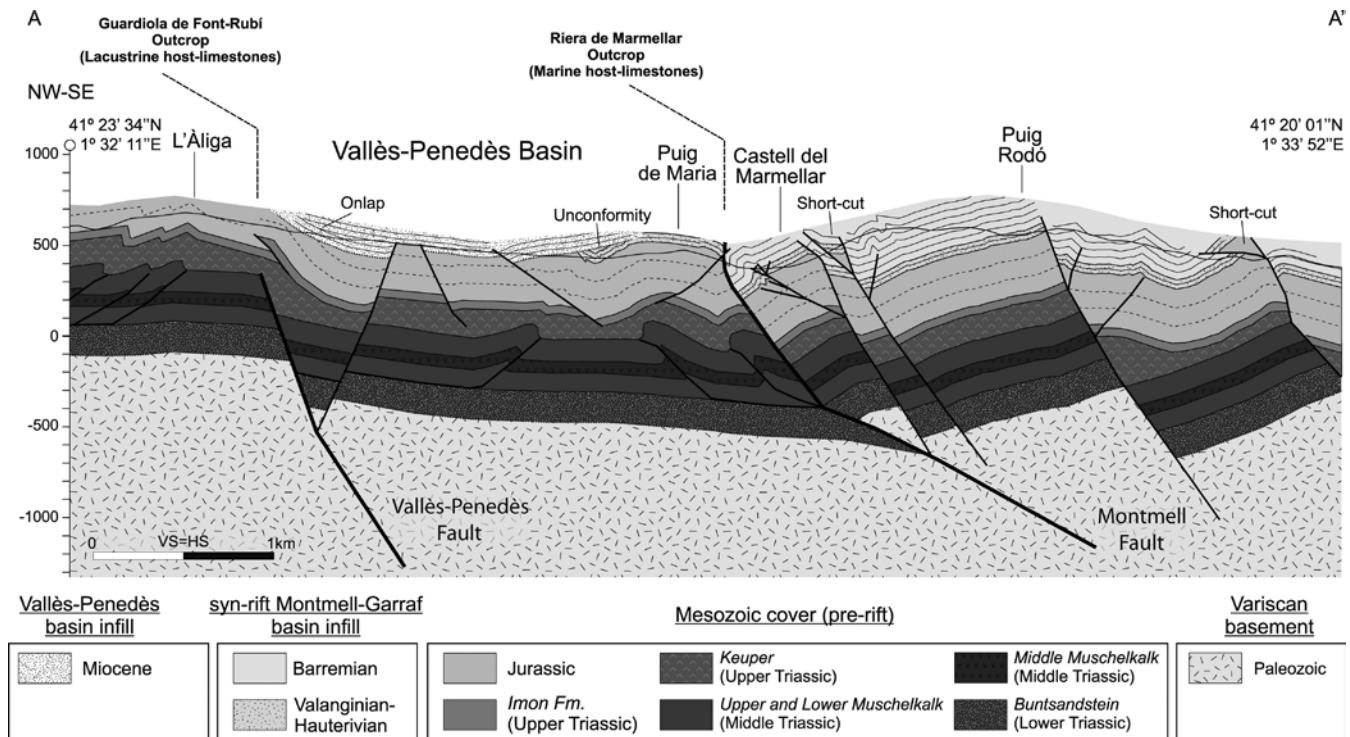


Fig. 3. Geological cross-section through the Vallès-Penedès and Montmell faults. The Riera de Marmellar and Guardiola de Font-Rubí outcrops have been projected to their equivalent structural position.

southern Montmell realm, belonging to the NW margin of the Garraf-Montmell Basin, made up by a complete Mesozoic succession with a thick Upper Jurassic–Lower Cretaceous succession; and the northern Gaia realm in which the Mesozoic is much thinner and represented only by Triassic rocks unconformably covered by lower Paleogene sediments of the Ebro Basin margin (Anadón *et al.* 1979).

A cross-section through the boundary between these two realms (Fig. 3) depicts that the structure of the study area is controlled by the motion of a series of SE-dipping basement extensional faults and by the presence of an Upper Triassic ductile level that decouples the deformation. Among the basement faults the Vallès-Penedès and the Montmell faults are notable. The first one is an extensional fault that, along the presented section, dies out in the Upper Triassic interval and drape folds the overlying Jurassic and Miocene rocks. Growth strata geometries in the Miocene sediments, as well as the fold geometry of the underlying Jurassic rocks, denote that its main extensional motion occurred during the Miocene. The other one, the Montmell Fault, bounds NW of the thick Upper Jurassic–Lower Cretaceous infill of the Garraf-Montmell Basin. It cuts all the Mesozoic successions but not the Miocene basin infill of the Vallès-Penedès half-graben which, northeastwards of the cross-sectional trace (Fig. 2), unconformably overlies the fault. The offset of the fault is extensional on the upper part but contractional on Lower Triassic–Palaeozoic levels. The boundary between these two parts coincides with a concave fault dip change and with the branch line of a hinterland-dipping duplex developed at the footwall block. This geometry is typical in inversion tectonics and corresponds to the contractional reactivation of an extensional fault with a footwall short-cut formation (Cooper *et al.* 1989). Supporting this interpretation, SE of the Montmell Fault, the Jurassic and Lower Cretaceous Garraf-Montmell Basin fill appears deformed by several parallel extensional faults with clear footwall short-cuts and SE-directed thrusts and folds that

can be interpreted as buttressing structures developed against the extensional fault (Gillcrust *et al.* 1987). Taking into account that all these structures do not affect the Neogene infill of the Vallès-Penedès half-graben, the extensional motion of the Montmell Fault is attributed to be Late Jurassic–Cretaceous (coeval to the formation of the Garraf-Montmell Basin) and the contractional fault reactivation to the Paleogene (Marin *et al.* 2008).

To ascertain the movement of fluids during the Mesozoic formation and later Cenozoic contractional and extensional reactivations of the major basement faults present in the central part of the Catalan Coastal Ranges, two outcrops have been chosen, one located at the Montmell Fault and the other at the Vallès-Penedès Fault (see Figs 2, 3).

METHODOLOGY

The paragenetic sequence of diagenetic events was deduced from field and petrographic observations. Geochemical characteristics of consecutive diagenetic products then allowed subdividing the paragenesis of fluid flow history into four different stages. Finally, it was possible to link the paragenesis to the kinematic history obtained from the macro- and microstructural study. Diagenetic products (calcite cement and sediments infilling fractures) and the host rocks (marine and lacustrine limestones) were sampled in the two outcrops. Twenty-two samples of the host rock and different generations of veins infilling faults were collected. The samples were cut, polished and 40 thin sections were selected. The thin sections were stained with Alizarine Red-S and potassium ferricyanide to distinguish calcite and dolomite and their ferroan equivalents (Dickson 1966) and later they were studied using optical and cathodoluminescence microscopes. A Technosyn Cold Cathodoluminescence device (model 8200 MkII) operating at 15–18 KV and a 150–350 μ A gun current was used.

The calcite cements from the host rock and fractures were sampled for carbon- and oxygen-isotope analysis employing a 500 μm thick dental drill to extract $60\pm 10\ \mu\text{g}$ of powder from polished slabs. The powdered calcite was reacted with 103% phosphoric acid for 2 min at 70°C . The CO_2 was analysed using an automated Kiel Carbonate Device attached to a Thermal Ionization Mass Spectrometer Thermo Electron (Finnigan) MAT-252. The results are precise to $\pm 0.02\%$ for $\delta^{13}\text{C}$ and $\pm 0.04\%$ for $\delta^{18}\text{O}$. The results were corrected using the standard technique of Craig & Gordon (1965) and Claypool *et al.* (1980) and are expressed in ‰ with respect to the VPDB standard.

Sr chromatography was performed using the method described by Pin & Bassin (1992) using Sr resin commercially known as *Sr-Spec* and elaborated by Eichrom. Sr isotope measurements were carried out in a mass spectrometer Finnigan MAT-262 from the Department of Isotope Geochronology and Geochemistry of SGIker of the University of the Basque Country. Samples were loaded on to a Ta filament (99.95%) previously degassed in two stages at 2 A and 4.5 A for 30 minutes. The measurement of isotopic ratios was made in the following conditions: ^{88}Sr beam intensity approx. 4V, acquiring 20 blocks of 10 sweeps, and ^{85}Rb being used to monitor potential isobaric interferences. The analytical data were corrected by linear law mass fractionation using as a constant ratio $^{87}\text{Sr}/^{86}\text{Sr} = 0.1194$ (Steiger & Jäger 1977).

Carbon-coated polished thin-sections were used to analyse minor and trace element concentrations on a CAMECA SX-50 electron microprobe. The microprobe was operated using 20 KV of excitation potential, a current intensity of 15 nA and a beam diameter of 10 μm . The detection limits are 100 ppm for Mn, 145 ppm for Fe, 100 ppm for Na, 400 ppm for Mg, 90 ppm for Sr and 500 ppm for Ca.

STRUCTURAL AND MICROSTRUCTURAL DATA

Two locations that lie about 15 km apart from each other were selected in accordance with their structural position in the general cross-section through the Montmell and the Vallès-Penedès Faults (Fig. 3): the Riera de Marmellar outcrop (RMO) and the Guardiola de Font-Rubí outcrop (GFRO). The RMO is located within the Montmell Fault hanging wall (central part of the Montmell realm), whereas the GFRO is located in the western sector of the Vallès-Penedès Fault zone. In the RMO the host rocks are Lower Cretaceous marine limestones comprising 1–4 m thick beds, trending NE–SW and dipping 30° to the NW whereas in the GFRO the host rocks are Lower Cretaceous lacustrine limestones comprising 1–3 m thick vertical beds with roof brands and oxides at the strata top, giving a yellowish tinge to the rock (Fig. 4a, b). In both outcrops, the limestones contain metric-scale faults, micro-faults and tension veins filled with calcite cements and numerous stylolite surfaces. The macrostructural data were displayed on stereo-plots and have been grouped in different phases according to their relative chronology (Fig. 5).

- The first phase of deformation is represented by type 1 fractures. These fractures correspond to tension veins that form a complex network. They have been divided into type 1a fractures, which are sub-parallel to bedding, and type 1b fractures, which cut at 30° the type 1a fractures.
- The second phase of deformation has been divided into three sub-groups. In the RMO, fractures type 2a and 2b trend N60 and dip $60\text{--}80^\circ$ to the NW and SE. The type 2b fractures are normal and reverse faults. The normal faults have a general orientation N60/80 NW with 80°W of slip and the reverse

faults have a general orientation N70/75 SE with a 70°E of slip. These normal and reverse fault orientations were restored to their original geometry by rotating bedding to horizontal; the reverse faults restore as normal-sense faults, without evidence of reactivation (Wibberley *et al.* 2007). These normal faults have a high angle of dip because of their rotation in close proximity to the Montmell Fault. The last generation is type 2c fractures, trending N15 and dipping 60° to the east. In the GFRO only fracture type 2a is present, trending N150 and dipping 70° to the west.

- The third phase of deformation is characterized by type 3 fractures, which are present in both outcrops. They correspond to reverse faults trending N60 and dipping $70\text{--}85^\circ$ to the SE and NW with $75\text{--}90^\circ$ east and west slickenlines. In the GFRO, these faults are cut by another set of reverse faults trending N55 and dipping 25° to the NW with a slip of 54° to the east.
- The fourth deformation stage is characterized by the type 4 fractures, only present in the RMO. These fractures correspond to sub-vertical tension gashes trending N130 and sometimes displaying a sigmoid morphology consistent with a normal motion. They are recognized at meso- and micro-scale.
- The fifth deformation stage is characterized by the type 5 fractures, only present in the GFRO. They are normal faults trending N–S to NE–SW and dipping $60\text{--}70^\circ$ to the SE and NW with a slip of 25° south for the N–S-trending faults and 70° west for the NE–SW trending faults. Other macro-fractures with the same trend and dip have been recognized; however, the slickenlines are absent.
- Finally the last deformation stage is characterized by the type 6 fractures. They are present in the GFRO and correspond to sub-vertical tension fractures trending NNW–SSE.

PETROLOGY AND GEOCHEMISTRY

The marine host-limestones correspond to wackestone, packstone and grainstone of miliolids, peloids, orbitolines, rudists and ostreids, whereas the lacustrine host-limestones correspond to a wackestone–packstone of charophyta, ostracoda and gasteropoda fragments. In both cases, the intragranular porosity is filled by microsparite cement (C0a) and the luminescence of the limestones is red to orange. Compositional data are summarized in Table 1 and isotopic data are cross-plotted in Figures 6 and 7.

The calcite cement C0a consists of anhedral crystals, 5–10 μm in size, red to orange luminescent. The elemental composition of this cement is similar to the host limestones (see Table 1).

The limestones are brecciated, probably during the initial fluid loss of the sediment, giving weak differences in luminescence and are affected by an incipient process of dolomitization. The dolomitization process is characterized by the presence of individualized rhombohedral crystals (CD1), 100–200 μm in size, non-luminescent, although locally the nucleus shows an orange dull luminescence. The dolomite crystals have been later calcitized (see Table 1).

A partial dissolution of the rock has created moldic and vug porosity. This porosity was partially filled by micrite and the remaining porosity was occluded by the calcite cement C0b showing geopetal disposition. The cement C0b corresponds to euhedral calcite crystals featuring blocky texture, 100–500 μm in size and showing a zoned red to orange luminescence.

Different generation of breccias, cements and sediment infillings have been recognized related to the fractures described in the structural section. These diagenetic products are described following the same chronological order of the different deformations stages.

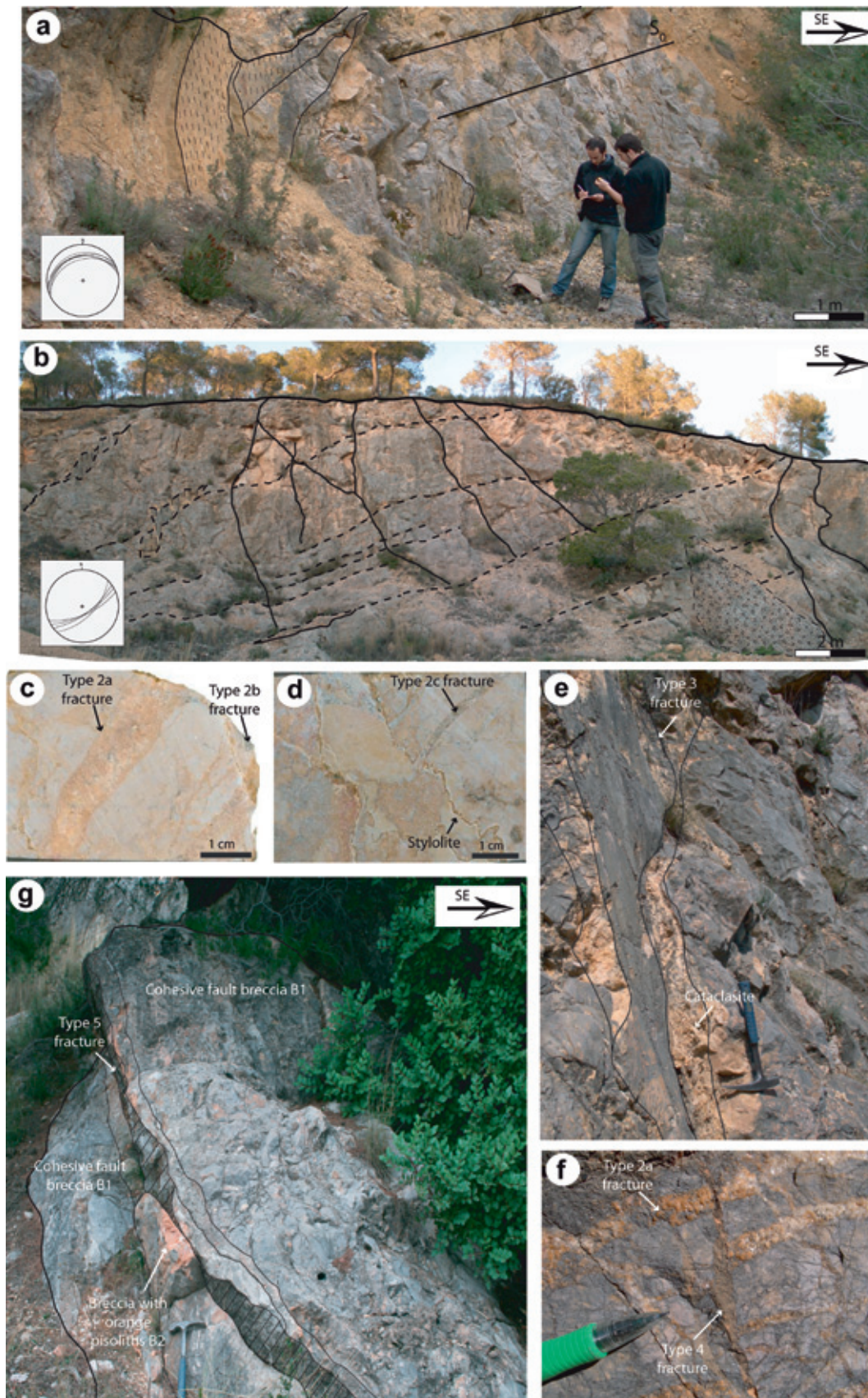


Fig. 4. (a) Riera de Marmellar outcrop showing the main normal faults (fractures type 2b) (dashed lines) and bedding planes (continuous lines); (b) Guardiola de Font-Rubí outcrop showing the main reverse faults (fractures type 3) (dashed lines) and main normal faults (fractures type 5) (continuous lines); (c) hand specimen showing type 2a and 2b fractures; (d) hand specimen showing type 2c fractures and random stylolites (stylobreccia); (e) slip surface of type 3 fractures and related yellow cataclasite; (f) outcrop photograph showing type 2c and type 4 fractures; (g) slip surface of type 5 fractures and related cohesive fault breccia B1 and breccia with orange pisoliths B2.

online
colour
only

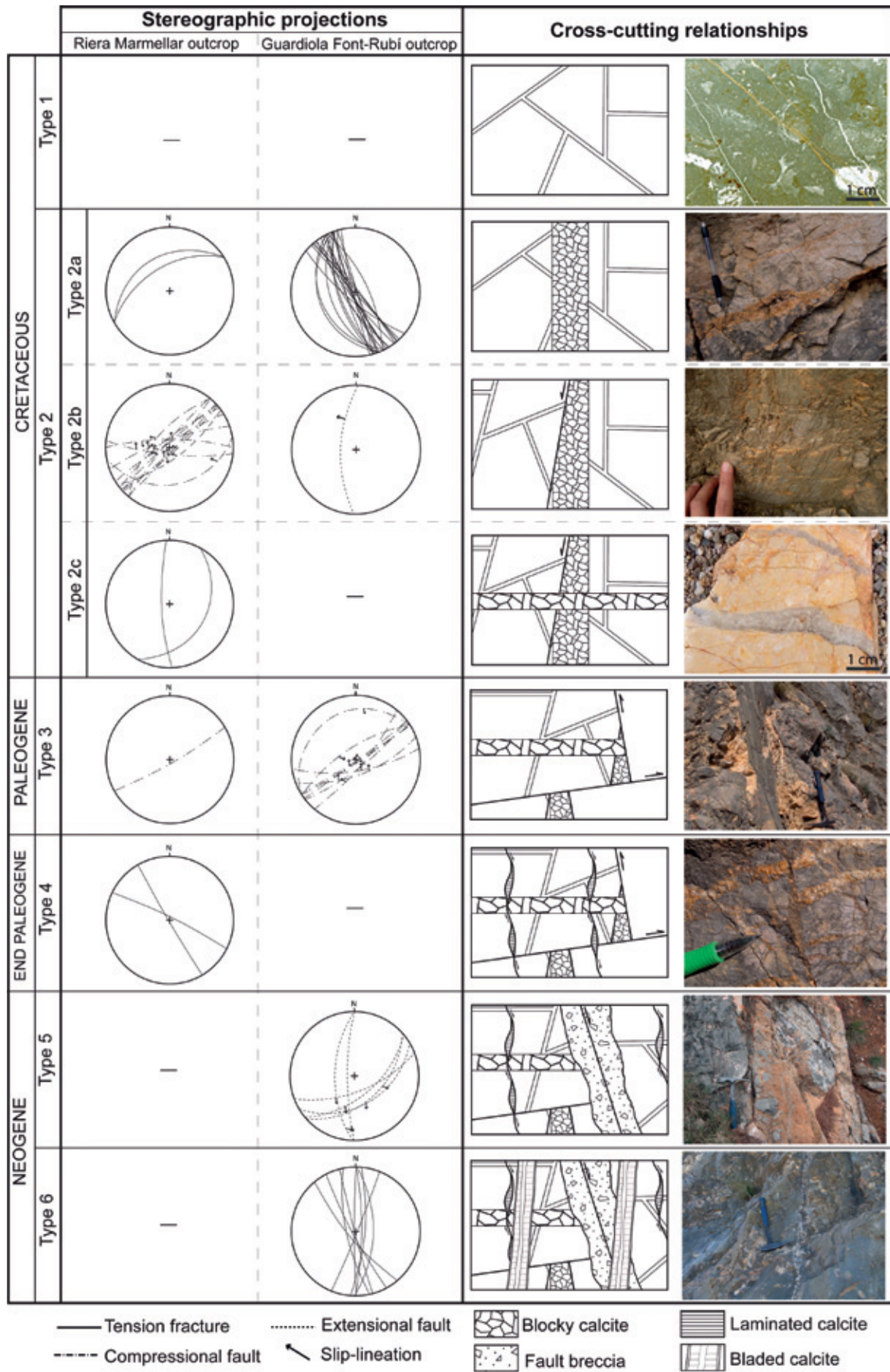


Fig. 5. Stereo-plots of structural and microstructural data from Riera de Marmellar and Guardiola de Font-Rubi outcrops.

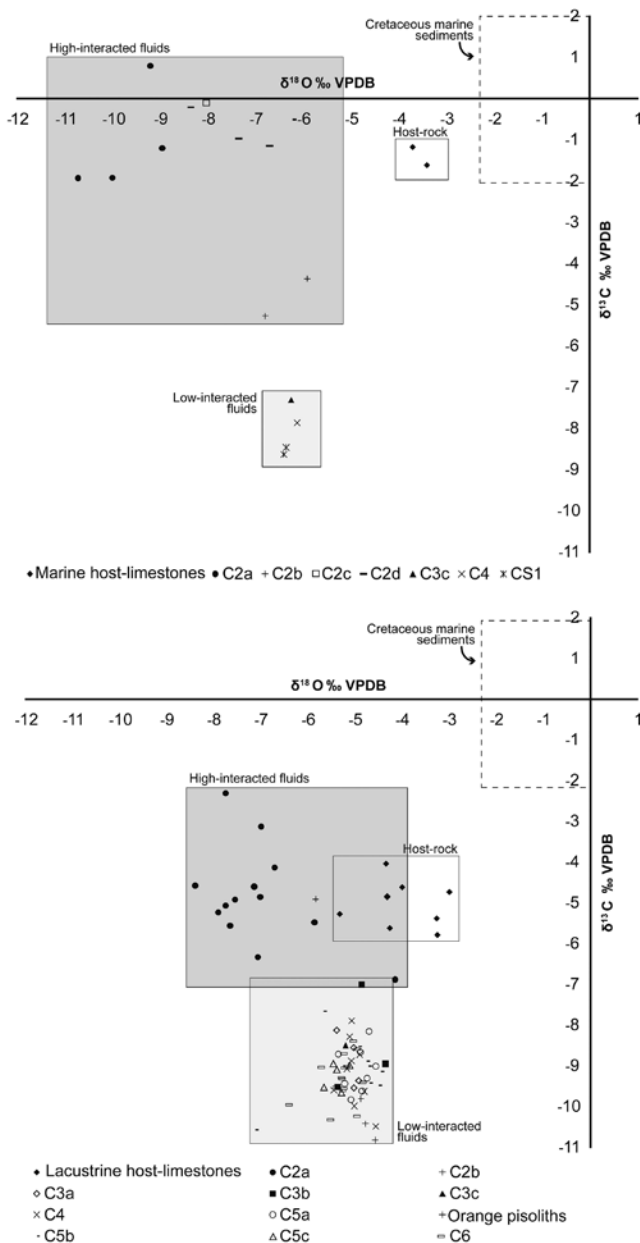


Fig. 6. $\delta^{18}\text{O}$ and $\delta^{13}\text{C}$ cross-plot of the host limestones and calcite cements and sediments. Range of values for Cretaceous marine sediments after Veizer & Hoefs (1976).

Type 1 fractures and calcite cement C1

Type 1a fractures are 25–50 μm in width and the walls are irregular and enlarged by dissolution. They are filled by two generations of calcite cement. The first generation (C1a) forms a rim, up to 10 μm thick, in one of the fracture walls. The crystals, 5–10 μm in size, are subhedral with c-axes orientated perpendicular to the fracture wall. They are zoned, from non-luminescent to orange bright luminescent. The second cement generation (C1b) is formed by dull-orange luminescent euhedral crystals, 10–15 μm in size, forming a mosaic fabric. Type 1b fractures are filled by the same type of calcite mosaic fabric with dull-orange luminescence (C1b) (Figs 8a, b). The elemental composition of these fillings is variable (see Table 1).

Type 2 fractures and calcite cement C2

Due to the similarities in the geochemistry and structural data, this group includes type 2a, 2b and 2c fractures, each with different types of fillings.

Type 2a fractures and calcite cement C2a and C2b. Type 2a fractures are 500 μm to 5 cm wide and have straight walls (Fig. 4c). They contain two generations of filling: the first corresponds to calcite cement C2a. This calcite has a milky aspect in hand sample and is constituted by subhedral crystals 300 μm to 1.5 mm in size, with a red dull luminescence featuring a drusy texture. The cloudy appearance of these crystals is due to abundant solid inclusions and mechanical twin planes (Figs 8c, d). Locally the crystals are elongated, growing with the c-axis perpendicular to the fracture walls, giving a bladed texture. The second generation of filling corresponds to calcite cement C2b. This calcite is translucent orange in hand sample. The crystals are euhedral, 100 μm to 1.5 mm in size, have a cloudy appearance due to abundant solid inclusions and mechanical twin planes, with a red dull luminescence and have a drusy texture.

Type 2b fractures and calcite cement C2c. The striated calcite cement present along the type 2b fault planes (calcite cement C2c) is constituted by subhedral to euhedral crystals, 100–500 μm in size, featuring a blocky texture. The crystals contain abundant mechanical twin planes and are red dull to red bright luminescent. Closer to the fault plane this calcite becomes a microsparite, 70–100 μm in size, corresponding to the cataclasis of the bigger calcite crystals (Fig. 8e).

Type 2c fractures and calcite cement C2d. Type 2c fractures are open, from 500 μm to 1 cm wide and have sub-angular walls enlarged by dissolution (Fig. 4d). They contain one generation of calcite cement C2d. This calcite has a white translucent aspect in hand sample and is composed of euhedral crystals, 75 μm to 1 mm in size, with a zoned black-orange bright-black luminescence, and a drusy texture (Figs 8a–e).

Type 3 fractures and calcite cement C3

Related to type 3 fractures is a fault zone over 0.5 m thick. The *core zone* is comprised of a yellow cataclasite (Fig. 4e), formed by fragments of the host limestones and earlier cements, 0.1–0.5 cm in size. The cataclasite has two generations of calcite cement: the first generation of cement (C3a) contains anhedral, non-luminescent, microsparite crystals, 4–10 μm in size, featuring blocky texture. The second generation of cement (C3b) surrounds sub-rounded fragments of the cataclasite, 0.1–2 cm in size. This cement consists of euhedral non-luminescent crystals, 10–100 μm in size, featuring blocky texture (Fig. 8f).

Later movements of the reverse faults generated the cataclasis of the earlier cataclasites and cements and a syn-kinematic striated calcite precipitated along the fault planes. This calcite cement (C3c) corresponds to non-luminescent, euhedral crystals, 200–500 μm in size, featuring blocky texture. The crystals are highly deformed and contain abundant mechanical twins planes (Fig. 7f).

Stylolites and breccias

The stylolite system is comprised of mostly open and randomly orientated stylolites (from sub-horizontal to sub-vertical), giving

Table 1. (Continued)

Filling stage	Luminescence		$\delta^{13}\text{C}$ (‰) VPDB)	$\delta^{18}\text{O}$ (‰) VPDB)	$^{87}\text{Sr}/^{86}\text{Sr}$	Mg (%)	Ca (%)	Na (ppm)	Mn (ppm)	Fe (ppm)	Sr (ppm)	Molar ratio Mg/Ca fluid (a)	Molar ratio Mg/Ca fluid (b)	Molar ratio Sr/Ca fluid (c)	Molar ratio Sr/Ca fluid (d)	Molar ratio Ca/Fe fluid (e)
Calcite cement C3a (GFRO) ($n = 16$)	Non-luminescent	m	-9.4	-5.4	—	< d.l.	39.25	< d.l.	< d.l.	< d.l.	< d.l.	—	—	—	—	—
		M	-8.1	-4.9	—	0.18	40.15	447	59	811	375	0.6376	0.0658	0.0160	0.0054	4804.6
		mv	-8.9	-5.1	—	—	39.70	—	—	—	—	—	—	—	—	—
Calcite cement C3b (GFRO) ($n = 12$)	Non-luminescent	m	-9.5	-5.4	—	< d.l.	39.46	< d.l.	< d.l.	< d.l.	< d.l.	—	—	—	—	—
		M	-7.0	-4.4	—	0.26	40.564	228	312	247	535	0.8995	0.0928	0.0227	0.0077	942
		mv	-8.4	-4.9	—	—	40.00	—	—	—	—	—	—	—	—	—
Calcite cement C3c (GFRO) ($n = 5$)	Non-luminescent	m	—	—	—	0.09	39.15	< d.l.	< d.l.	< d.l.	< d.l.	0.3049	0.0315	—	—	—
		M	—	—	—	0.20	40.85	128	79	105	293	0.6998	0.0722	0.0125	0.0042	3903.1
		mv	-8.5	-5.2	0.70791	0.15	40.01	—	—	—	—	0.5078	0.0524	—	—	—
Calcite cement C3c (RMO) ($n = 1$)	Non-luminescent	m	—	—	—	—	—	—	—	—	—	—	—	—	—	—
		M	—	—	—	—	—	—	—	—	—	—	—	—	—	—
		mv	-7.3	-6.3	—	—	—	—	—	—	—	—	—	—	—	—
Calcite cement C4 (GFRO) ($n = 13$)	Non-luminescent	m	-10.5	-5.5	—	0.11	39.28	< d.l.	< d.l.	< d.l.	< d.l.	0.3734	0.0385	—	—	—
		M	-7.9	-4.6	—	0.41	40.55	108	94	1351	617	1.4234	0.1469	0.0266	0.0090	14034
		mv	-9.2	-5.0	—	0.23	39.92	—	—	—	—	0.7788	0.0804	—	—	—
Calcite cement C4 (RMO) ($n = 9$)	Non-luminescent	m	—	—	—	0.01	40.14	< d.l.	< d.l.	< d.l.	154	0.0327	0.0034	0.0065	0.0022	—
		M	—	—	—	0.16	40.68	161	141	112	651	0.5391	0.0556	0.0274	0.0092	3903
		mv	-7.9	-6.1	—	0.08	40.35	—	—	—	—	0.2612	0.0270	0.0138	0.0046	—
Calcite sediment CS1 (RMO) ($n = 3$)	Non-luminescent	m	-8.6	-6.4	—	0.10	39.40	< d.l.	< d.l.	1289	246	0.3557	0.0367	0.0104	0.0035	54.8
		M	-8.5	-6.4	—	0.18	40.24	110	23	2009	382	0.6332	0.0653	0.0162	0.0055	86.5
		mv	-8.5	-6.4	0.70809	0.14	39.84	—	—	1663	308	0.4673	0.0482	0.0131	0.0044	69.6
Calcite cement C5a (GFRO) ($n = 25$)	Non-luminescent	m	-9.8	-5.4	—	< d.l.	39.13	< d.l.	< d.l.	< d.l.	< d.l.	—	—	—	—	—
		M	-6.9	-4.1	—	0.53	40.499	220	103	1748	578	1.8535	0.1912	0.0245	0.0083	1311
		mv	-8.8	-4.8	—	—	39.63	—	—	—	—	—	—	—	—	—
Orange pisoliths (GFRO) ($n = 4$)	Non-luminescent	m	-10.8	-4.9	—	0.05	38.96	< d.l.	< d.l.	462	< d.l.	0.1768	0.0182	—	—	52.9
		M	-9.8	-4.6	—	0.16	40.56	150	51	2056	255	0.5649	0.0583	0.0109	0.0037	239.4
		mv	-10.3	-4.7	—	0.11	39.69	—	—	1095	—	0.3952	0.0408	—	—	154.3
Calcite cement C5b (GFRO) ($n = 5$)	Non-luminescent	m	-10.3	-7.1	—	0.13	40.08	< d.l.	< d.l.	< d.l.	< d.l.	0.4537	0.0468	—	—	—
		M	-8.5	-4.4	—	0.19	40.497	215	175	210	333	0.6677	0.0689	0.0140	0.0047	1561
		mv	-9.2	-5.2	—	0.17	40.28	—	—	—	—	0.5681	0.0586	—	—	—
Calcite cement C5c (GFRO) ($n = 13$)	Non-luminescent	m	-9.7	-5.7	—	< d.l.	39.42	< d.l.	< d.l.	< d.l.	< d.l.	—	—	—	—	—
		M	-9.0	-5.1	—	0.25	40.58	160	92	125	332	0.8747	0.0903	0.0139	0.0047	4128
		mv	-9.3	-5.4	0.70825	—	40.13	—	—	—	—	—	—	—	—	—
Calcite sediment CS2 (GFRO) ($n = 8$)	Non-luminescent	m	—	—	—	< d.l.	39.16	< d.l.	< d.l.	124	< d.l.	—	—	—	—	67.5
		M	—	—	—	0.18	39.94	373	77	1643	361	0.6261	0.0646	0.0153	0.0052	898.6
		mv	—	—	—	—	39.60	—	—	677	—	—	—	—	—	383.7
Calcite cement C6 (GFRO) ($n = 28$)	Non-luminescent	m	-10.2	-6.3	—	0.07	39.50	< d.l.	< d.l.	< d.l.	< d.l.	0.2446	0.0252	—	—	—
		M	-8.4	-4.9	—	0.69	40.577	4246	809	353	500	2.3708	0.2446	0.0213	0.0072	15898
		mv	-9.3	-5.4	—	0.25	40.01	—	—	—	—	0.8673	0.0895	—	—	—

m, minimum value; M, maximum value; mv, mean value; n , number of elemental analysis spots in the same sample; < d.l., below detection limit

^aKMg = 0.012 at 25°C (Mucci 1987)

^bKMg = 0.1163 at 90°C (Katz 1973)

^cKSr = 0.027 at 25°C (Lorens 1981)

^dKSr = 0.08 at 100–150°C (Kinsman 1969)

^eKFe = 5 at 25°C (Tucker & Wright 1990)

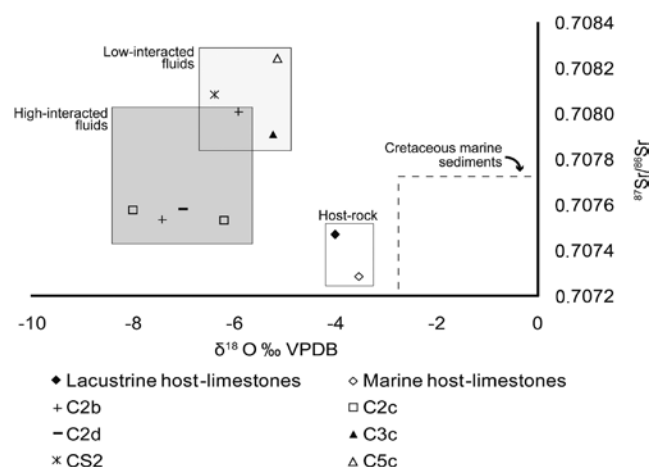


Fig. 7. Cross-plot of strontium ratio versus oxygen isotopic compositions of the host limestones and calcite sediments and cements.

the rock a pseudo-nodular texture, described as stylobreccia (Figs 4d, 8g) (*sensu* Stewart & Hancock 1990).

Type 4 fractures, calcite cement C4 and calcite sediment CS1

Type 4 fractures are 300 μm to 5 cm wide and have sub-angular walls, enlarged by dissolution (Fig. 4f). They contain two generations of calcite fillings. The first generation corresponds to the calcite cement C4 formed by white translucent calcite in hand specimen, comprised of euhedral non-luminescent crystals, 100–200 μm in size, featuring blocky texture. The second generation of filling corresponds to the orange- to pink-laminated calcite sediment CS1. This sediment is comprised of non-luminescent euhedral crystals, 10–50 μm in size, featuring blocky texture. The sediment contains reworked fragments of the host limestone and earlier cements, 0.1–3 cm in size.

Type 5 fractures and calcite cement C5

A different generation of fault breccias were developed in association with type 5 fractures (Fig. 4g). Cohesive fault breccia B1 is formed by angular fragments, between 0.1 cm and 3 cm in size, of host limestone and earlier calcite cements. This breccia is cemented by calcite cement C5a, comprised of non-luminescent anhedral calcite crystals, 10–20 μm in size, featuring blocky texture (Fig. 8h). In the central part of the core zone, there is a breccia with orange pisoliths B2 (Fig. 8i). This breccia is formed from sub-rounded fragments, 1–5 cm in size, of the host rock, calcite cements and cohesive fault breccia B1. Some of the fragments are coated by an orange micrite and between the fragments orange pisoliths are present. These pisoliths are 10–50 μm in size and their nucleus have been totally micritized. The breccia B2 is cemented by the calcite cement C5b. This cement is formed from non-luminescent euhedral crystals, 50–200 μm in size, featuring blocky texture (Fig. 8i).

Later movements of the normal faults caused the cataclasis of breccia B2. Synchronous with the movement of the normal faults, calcite cement C5c was precipitated (Fig. 8j). This cement shows crack-seal structures with inclusion bands of orange pisoliths and locally sigmoidal morphology. C5c is formed from

non-luminescent subhedral to euhedral crystals, 250–500 μm in size, featuring blocky texture. The crystals contain abundant mechanical twin planes.

Type 6 fractures, calcite sediment CS2 and calcite cement C6

Type 6 fractures are 5–10 cm in width, with sharp and undulating walls and are partially filled by two generations of calcite sediment and cement. The first generation corresponds to pink-laminated calcite sediment CS2. The sediment is comprised of non-luminescent, subhedral crystals, 10–30 μm in size, featuring blocky texture (Fig. 8k). The second generation of filling is the calcite cement C6. This cement is comprised of non-luminescent bladed crystals, 500 μm to 2 cm in size, with the c-axis perpendicular to the fracture wall (Fig. 8k).

DISCUSSION

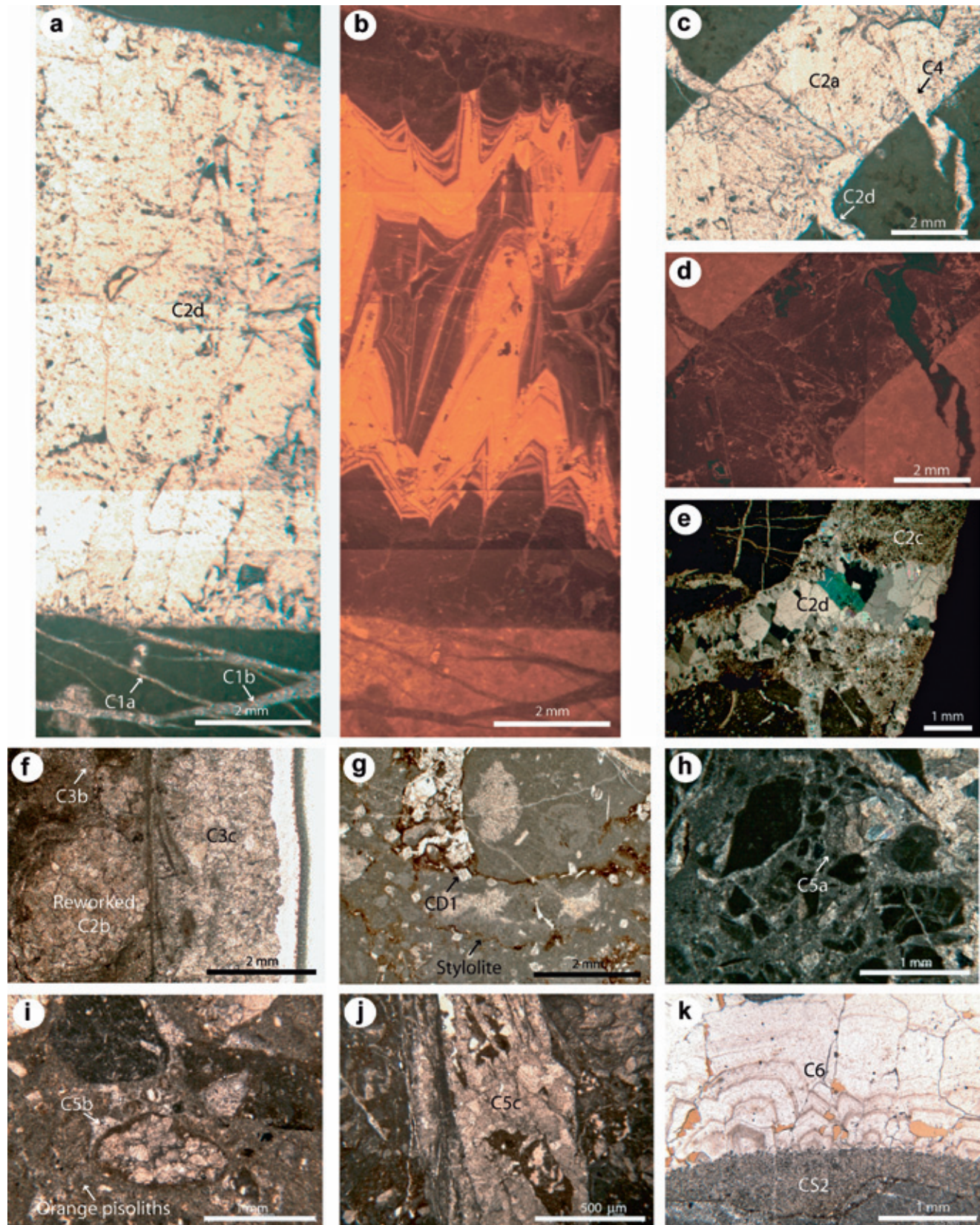
Diagenesis of host limestones

If it is assumed that the precipitation of the calcite cement occurred in equilibrium, the chemical composition of the fluid responsible for the calcite precipitation can be determined using the distribution coefficient equation of McIntire (1963). The molar ratios Ca/Fe, Mn/Ca and Sr/Ca of the host marine limestone and the intraparticle cement C0a are consistent with re-equilibration and precipitation from formation waters, whereas the molar ratios of Mg/Ca are consistent with re-equilibration and precipitation from either meteoric or formation waters. The $\delta^{18}\text{O}$ values of the host marine limestone are slightly lower than the expected values for limestones precipitated from the Cretaceous seawater (from -2.5 to +1‰ VPDB), whereas the $\delta^{13}\text{C}$ and the strontium ratios are in good agreement with those of limestones precipitated from Cretaceous seawater, ranging from -2 to +3‰ VPDB and from 0.7068 to 0.7074, respectively (Veizer & Hoefs 1976; Veizer *et al.* 1997, 1999). These data show that the original marine signal is still recognized for $\delta^{13}\text{C}$ and the strontium ratio but it has been moderately overprinted during diagenesis, modifying the $\delta^{18}\text{O}$ values. On the other hand, the molar ratios Sr/Ca, Ca/Fe and Mg/Ca and the $\delta^{18}\text{O}$ and $\delta^{13}\text{C}$ values of the lacustrine host limestone and calcite cement C0a clearly show a meteoric origin for the fluid (from -8 to -2‰ $\delta^{18}\text{O}$ VPDB and from -12 to 0‰ $\delta^{13}\text{C}$; Veizer & Hoefs 1976). The geochemistry of the intraparticle cement C0a indicates, in both cases, precipitation during the very early stages of diagenesis.

The molar ratios Mg/Ca and Sr/Ca of CD1 and C0b in the marine limestones clearly indicate precipitation from formation waters, whereas in the lacustrine limestones they are consistent with meteoric waters. These values indicate that dissolution, brecciation, incipient dolomitization and subsequent calcitization of the dolomite crystals, as well as precipitation of cement in the vug and moldic porosity, occurred during initial burial of the rock and, therefore, the initial stages of mesogenesis.

Relationships between fracturing events and palaeofluids

Knowing the regional setting of the study area it is possible to correlate the different fracturing stages to the main tectonic events (Knipe & McCaig 1994). The different fractures, breccias



online
colour
only

Fig. 8. (a), (b) Type 1a, 1b and 2c fractures with C1a, C1b and C2d calcite cements under (a) optical and (b) cathodoluminescence microscope; (c), (d) type 2a, 2c and 4 fractures with C2a, C2d and C4 calcite cements under (c) optical and (d) cathodoluminescence microscope; (e) type 2b and 2c fractures with C2c and C2d calcite cements under optical microscope; (f) type 3 fractures with related cataclasite and C3b calcite cement under optical microscope; (g) stylobreccia related to type 3 fractures under optical microscope. Detail of the dolomite crystals (CD1); (h) cohesive fault breccia B1 related to type 5 fractures with the calcite C5a under optical microscope; (i) breccia with orange pisoliths B2 cemented by C5b under optical microscope; (j) cataclasite of breccia B2 with the calcite cement C5c under optical microscope; (k) type 6 fractures with the calcite sediment CS2 and calcite cement C6 under optical microscope.

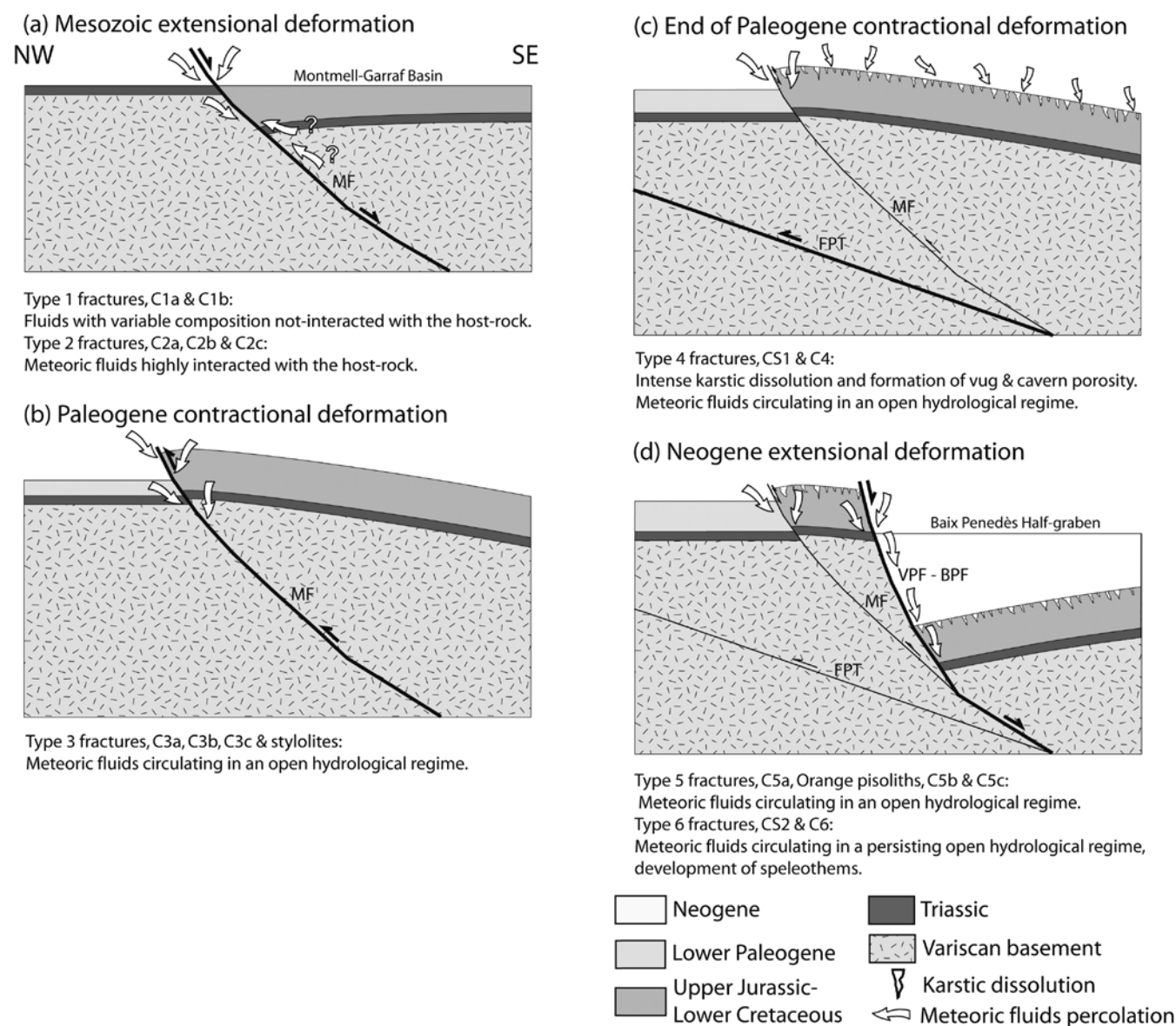


Fig. 9. Evolution of meteoric fluids from Mesozoic to recent within the Vallès-Penedès–Montmell Alpine fault system. MF, Montmell Fault; FPT, Frontal Paleogene Thrust; VPF–BPF, Vallès-Penedès Fault and Baix Penedès Fault.

and cementation processes observed along the NW border of the Penedès Basin attest to different fluids circulating during basin development.

Mesozoic extensional deformation. The complex network of type 1 fractures formed during the initial stage of Mesozoic extension. They represent the process zone formed around the fault tip during its development (Stewart & Hancock 1990). The large elemental composition range of calcite cements C1a and C1b suggests the infiltration of fluids of different compositions and origins, not interacted with the host limestone, during this multistage of fracturing (Fig. 9a).

During the Mesozoic extensional syn-rift stage, the NNW–SSE tension fractures (type 2a) and the NE–SW normal faults (type 2b) were formed. Petrological and geochemical similarities between calcites C2a, C2b and C2c related to type 2a and 2b fractures indicate that they precipitated from a fluid with the same origin. The molar ratios Mg/Ca, Sr/Ca and Ca/Fe of

these cements, both in marine and lacustrine limestones, are consistent with precipitation from formation waters. Because fractures in the RMO are from the hanging wall and those of the GFRO are from the footwall of the Montmell Fault, the more negative $\delta^{18}\text{O}$ values in the RMO are interpreted as having been precipitated at deeper burial depth. The similarity between the $\delta^{13}\text{C}$ values of C2a, C2b, C2c and the host rock is probably due to the buffering of pore-water carbon isotopic composition by extensive dissolution of the host limestones (Marshall 1992). The $^{87}\text{Sr}/^{86}\text{Sr}$ ratios, together with the $\delta^{13}\text{C}$ values, indicate high fluid–rock interaction in a closed palaeohydrological system. On the other hand, type 2c fractures can be related to the post-rift stage. The variations in luminescence of calcite cement C2d attest to a variability of fluid composition during its precipitation. The $\delta^{18}\text{O}$ values are consistent either with meteoric or formation waters, whereas the $^{87}\text{Sr}/^{86}\text{Sr}$ ratio and $\delta^{13}\text{C}$ values indicate high fluid–rock interaction in a closed palaeohydrological system.

In summary, cement C2 in type 2 fractures, related to the Mesozoic extensional phase, precipitated from a fluid that strongly interacted with the rock, approaching a closed system.

Paleogene contractional deformation. The reverse faults (type 3) and stylolites formed during the Paleocene to middle Oligocene contractional phase that generated the Catalan Intraplate Belt (Guimerà 2004). The Mg/Ca and Ca/Fe molar ratios, as well as the $\delta^{18}\text{O}$ and $\delta^{13}\text{C}$ of cements C3a, C3b and C3c in type 3 fractures and related cataclasite, are consistent with precipitation from meteoric water (Fig. 9b).

End of Paleogene contractional deformation. The vertical fractures (type 4) and their later enlargement by dissolution can be related to the subaerial exposure of the Mesozoic horsts and development of a karstic system during the transitional phase between Paleogene compression and Neogene extension (Fig. 9c). The elemental geochemistry and the more radiogenic isotopes of the calcite sediment CS1 indicate low interaction with the host limestone and the opening of the system to meteoric water. The Mg/Ca, Sr/Ca and Ca/Fe ratios, as well as the $\delta^{18}\text{O}$ and $\delta^{13}\text{C}$ values of the calcite cement C4, indicate precipitation from meteoric waters in an open hydrological system. Similar fractures, sediments and cements related to karstic processes have been described during this transitional phase within the Penedès Basin (Travé *et al.* 1998) and in the neighbouring Amposta offshore oil reservoir (Playà *et al.* 2010).

Neogene extensional deformation from late Oligocene (?) to late Neogene. The type 5 fractures corresponding to NE–SW normal faults are attributed to the syn-rift stage of the late Oligocene?–Neogene extensional phase (Roca & Guimerà 1992). The fillings of type 5 fractures are a mixture of tectonic and karstic processes and resulted from multistage movement of the normal faults. The location of frictional processes generated the cohesive fault breccia B1 and the cataclasite during progressive opening of the hydrological system. When the fault reached the surface, karstic features from the vadose and phreatic meteoric environment led to the formation of the red breccias B2, the karstic pisolithic layer and the breccias with pisoliths. Later movements of the normal faults generated the cataclasis of karstic deposits. The $\delta^{18}\text{O}$ values of calcite cements C5a, C5b and C5c, varying from -7 to -4.4% VPDB, together with the Mg/Ca and Sr/Ca molar ratios and the high radiogenic values of C5c, indicate that meteoric waters, not interacted with the host limestone, were responsible for precipitation of these cements (Fig. 9d).

Finally, the type 6 fractures are attributed to the late post-rift stage of the Neogene extension as a result of generalized tensile deformation of the whole area during the final stages of basin development. The $\delta^{18}\text{O}$ values of CS2 and C6 filling type 6 fractures, varying from -6.3 to -4.9% VPDB, together with the calculated Mg/Ca and Sr/Ca molar ratios of the fluid, indicate precipitation from meteoric waters. The laminated calcite sediment CS2, together with the palisade texture of the calcite cement C6, are interpreted as speleothems covering the fractures walls, in the vadose meteoric environment, similar to those described in Miocene materials (Travé & Calvet 2001). The low $\delta^{13}\text{C}$ of the calcite cement C6 indicates a higher involvement of soil-derived CO_2 (Travé *et al.* 1998; Breesch *et al.* 2009).

This reconstruction of the relationship between fractures and migration of fluids within the Vallès–Penedès extensional basin development has an economic interest because

this basin can be used as an analogue for the reservoirs placed offshore of the Valencia Trough (Esteban 1999; Playà *et al.* 2010). These reservoirs correspond to a paleokarst developed over the Mesozoic carbonates during the Paleogene to Neogene transition stage (Vera *et al.* 1988; Esteban 1991). In the Montmell realm, this karstic dissolution and infilling is related to the formation of type 4 fractures which are filled by the carbonate sediments CS1. Knowing in detail the fracturing and diagenesis that occurred in these rocks will help unravel the evolution and migration of the oil during the development of the basin.

CONCLUSIONS

Structural analyses indicate that Mesozoic normal faults were reactivated during the Paleogene as reverse faults. During the Neogene, different normal faults generated the actual disposition of the Catalan Coastal Ranges.

Based on petrological and geochemical analyses of the different generations of calcite cements associated with the different generations of fractures, different types of fluids have been identified: (1) related to the earlier stage of Mesozoic extension, type 1 fractures include a complex network of microscopic fractures filled by calcite cements that precipitated from fluids with variable composition uninteracted with the host rock. (2) During the syn-rift stage of Mesozoic extension, NE–SW- to ENE–WSW-trending normal faults (type 2 fractures) were filled by three generations of calcite cement that precipitated at different burial depths from fluids resulted either from a mixing of trapped Upper Jurassic–Lower Cretaceous seawater and meteoric water, or from buffered meteoric waters highly interacted with the host rock. (3) During the Paleogene contractional deformation, NE–SW reverse faults (type 3 fractures) with a fault gouge cemented by several generations of non-luminescent calcite cements precipitated from meteoric fluids in an open hydrological system. (4) The end of the Paleogene contractional deformation is represented by vertical fractures (type 4 fractures) that favoured dissolution and created vug and cavern porosity. These cavities are filled by calcite cement and sediment precipitated from meteoric fluids related to the subaerial exposure of the basement carbonate rocks during the transitional stage. (5) During the Neogene syn-rift stage, NNW–SSE- and NE–SW-trending normal faults (type 5 fractures) filled by non-luminescent cements precipitated from meteoric fluids. (6) During the late post-rift stage, NNW–SSE open fractures (type 6 fractures) with the walls covered by speleothems indicate a persistent hydrological regime to meteoric open fluids.

We have recognized, in the studied outcrops, a complex fluid history during the two extensional phases, different in the Mesozoic extension than in the Neogene extension. In contrast, the Paleogene compression is characterized by a very simple fluid history characterized by meteoric fluids in small reverse faults.

Finally, two different episodes of karst development have been identified; an early one developed previous to the Neogene extension, which is used by the Neogene faults to develop, and a late one, developed after the Neogene extension, that originated at the expense of the Neogene normal faults.

The isotopic and electron microprobe analyses were carried out at 'Centres Científics i Tecnològics' of the University of Barcelona and the strontium analyses at SGiker Geochronology Department of the Faculty of Science and Technology, University of País Vasco/EHU. We also thank Andrea Billi and the anonymous reviewer of *Petroleum Geoscience* for their accurate and constructive reviews of this paper.

This research was performed within the framework of I+D+I research projects CGL2010-18260 of the Grup Consolidat de Recerca 'Geologia Sedimentària' (2009 SGR-1458), the BES-2007-14935 grant and the CGL2007-66431-C02/BTE of the 'Grup de Recerca de Geodinàmica i Anàlisi de Conques' (2001 SGR-000074).

REFERENCES

- Amigó, J. 1986. *Estructura del massís del Gaià. Relacions estructurals amb les fosses del Penedès i del Camp de Tarragona*. PhD Thesis, University of Barcelona, Barcelona, Spain.
- Anadón, P., Colombo, F., Esteban, M., Marzo, M., Robles, S., Santanach, P. & Solé Sugrañes, L. 1979. *Evolució tectonoestratigràfica de los Catalánides*. *Acta Geológica Hispánica*, **14**, 242–270.
- Anadón, P., Cabrera, L., Guimerà, J. & Santanach, P. 1985. Paleogene strike-slip deformation and sedimentation along the southeastern margin of the Ebro Basin. In: Biddle, K.T. & Christie-Blick, N. (eds) *Strike-Slip Deformation, Basin Formation Sedimentation*. Special Publication of the Society of Economic Paleontologists and Mineralogists, **37**, 303–318.
- André, G., Hibsich, C., Fourcade, S., Cathelineau, M. & Buschaert, S. 2010. Chronology of fracture sealing under a meteoric fluid environment: Microtectonic and isotopic evidence of major Cenozoic events in the eastern Paris Basin (France). *Tectonophysics*, **490**, 214–228.
- Ashauer, H. & Teichmüller, R. 1935. *Die variszische und alpidische Gebirgsbildung Kataloniens*. Abhandlungen Gesellschaft Wissenschaften Göttingen, Math Phys. Kl, **3F**, 16.
- Bartrina, M.T., Cabrera, L., Jurado, M.J., Guimerà, J. & Roca, E. 1992. *Evolution of the central Catalan margin of the Valencia trough (western Mediterranean)*. *Tectonophysics*, **203**, 219–247.
- Benedicto, A., Plagnes, V., Vergély, P., Flotté, N. & Schultz, R.A. 2008. Fault and fluid interaction in a rifted margin: integrated study of calcite-sealed fault-related structures (southern Corinth margin). In: Wibberley, C.A.J., Kurtz, W., Imber, J., Holdsworth, R.E. & Colletini, C. (eds) *The Internal Structure of Fault Zones: Implications for Mechanical and Fluid-flow Properties*. Geological Society, London, Special Publications, **299**, 1–19.
- Bitzer, K., Carmona, J.M., Calvet, F. & Travé, A. 1997. Modelling paleo-hydrological and thermal evolution of distensive basins: application to the Barcelona half-graben (offshore, NE Spain). In: Hendry, J., Carey, P., Parnell, J., Ruffell, A. & Worden, R. (eds) *Geofluids '97 Extended Abstracts*. Belfast, Northern Ireland, 352–355.
- Breesch, L., Swennen, R. & Vincent, B. 2009. Fluid flow reconstruction in hanging and footwall carbonates: Compartmentalization by Cenozoic reverse faulting in the Northern Oman Mountains (UAE). *Marine and Petroleum Geology*, **26**, 113–128.
- Bussolotto, M., Benedicto, A., Invernizzi, C., Micarelli, L., Plagnes, V. & Deiana, G. 2007. Deformation features within an active normal fault zone in carbonate rocks: The Gubbio fault (Central Apennines, Italy). *Journal of Structural Geology*, **29**, 2010–2037.
- Claypool, G.E., Holser, W.T., Kaplan, I.R., Sakai, H. & Zak, I. 1980. The age curves of sulphur and oxygen isotopes in marine sulphate and their interpretation. *Chemical Geology* (Isotope geoscience section), **28**, 199–260.
- Cooper, M.A., Williams, G.D. & De Graciansky, P.C. et al. 1989. Inversion tectonics – a discussion. In: Cooper, M.A. & Williams, G.D. (eds) *Inversion Tectonics*. Geological Society, London, Special Publications, **44**, 335–347.
- Craig, H. & Gordon, I. 1965. Deuterium and oxygen-18 variations in the ocean and marine atmosphere. In: Tongiorgi, E. (eds) *Stable Isotopes in Oceanographic Studies and Paleotemperatures*. Consiglio Nazionale delle Ricerche, Laboratorio di Geologia Nucleare, Pisa, Italy, 9–130.
- Dañobeitia, J.J., Arguedas, M., Gallart, F., Banda, E. & Makris, J. 1992. Deep crustal configuration of the Valencia trough and its Iberian and Balearic borders from extensive refraction and wide-angle reflection profiling. *Tectonophysics*, **203**, 37–55.
- De Brit, T.J. 1989. Timing structural events and basement emplacement using extension veins and cements in the Carboniferous of North Central Ireland. *Irish Journal of Earth Science*, **10**, 13–31.
- Dickson, J.A.D. 1966. Carbonate identification and genesis as revealed by staining. *Journal of Sedimentary Petrology*, **36**, 491–505.
- Fontboté, J.M. 1954. *Las relaciones tectónicas de la depresión del Vallès-Penedes con la cordillera prelitoral y con la depresión del Ebro*. Tomo Homenaje a Prof. E. Hernandez-Pacheco. Revista de la Sociedad Española de Historia Natural, Madrid, 281–310.
- Gaspar-Escribano, J., García-Castellanos, D., Roca, E. & Cloetingh, S. 2004. Cenozoic vertical motions of the Catalan Coastal Ranges (NE Spain): The role of tectonics, isostasy, and surface transport. *Tectonics*, **23**, DOI: 10.1029/2003TC001511.
- Gillcrist, R., Coward, M. & Mugnier, J.L. 1987. Structural inversion examples from the Alpine foreland and French Alps. *Geodinamica Acta*, **1**, 5–34.
- Guimerà, J. 1988. *Estudi estructural de l'enllaç entre la Serralada Ibèrica i la Serralada Costera Catalana*. PhD thesis, University of Barcelona, Barcelona, Spain.
- Guimerà, J. 2004. La Cadena Costera Catalana. In: Vera, J.A. (eds) *Geologia de España*. SGE-IGME, Madrid, 603–605.
- Katz, A. 1973. The interaction of magnesium with calcite during crystal growth at 25–90°C and one atmosphere. *Geochimica et Cosmochimica Acta*, **37**, 1563–1568.
- Kinsman, D.J.J. 1969. Interpretation of Sr²⁺ concentrations in carbonate minerals and rocks. *Journal of Sedimentary Petrology*, **39**, 486–508.
- Labauve, P., Carrio-Schaffhauser, E., Gamond, J.F. & Renard, F. 2004. Deformation mechanisms and fluid-driven mass transfers in the recent fault zones of the Corinth rift (Greece). *Comptes Rendus Géoscience*, **336**, 375–383.
- Llopis-Lladó, N. 1947. *Contribució al conocimiento de la morfoestructura de los Catalánides*. Inst. 'Lucas Madalla', C.S.I.C., Barcelona.
- Lorens, R.B. 1981. Sr, Cd, Mn and Co distribution coefficients in calcite as a function of calcite precipitation rate. *Geochimica et Cosmochimica Acta*, **45**, 553–561.
- Marín, M.A., Roca, E., Rosell, O., Marcuello, A. & Cabrera, L. 2008. La Falla del Montmell: un ejemplo del control ejercido por las fallas extensivas mesozoicas en la arquitectura cenozoica de las Cadenas Costaneras Catalanas. *Geotemas*, **10**, 461–464.
- Marshall, J.D. 1992. Climatic and oceanographic isotopic signals from the carbonate rock record and their preservation. *Geological Magazine*, **129**, 143–160.
- McIntie, W.L. 1963. Trace element partition coefficients – a review of theory and applications to geology. *Geochimica et Cosmochimica Acta*, **27**, 1209–1264.
- Micarelli, L., Benedicto, A., Invernizzi, C., Saint-Bezar, B., Michelot, J.L. & Vergely, P. 2005. Influence of P/T conditions on the style of normal fault initiation and growth in limestones from SE-Basin, France. *Journal of Structural Geology*, **27**, 1577–1598.
- Micarelli, L., Moretti, I., Jaubert, M. & Moulouel, H. 2006. Fracture analysis in the south-western Corinth rift (Greece) and implications on fault hydraulic behaviour. *Tectonophysics*, **426**, 31–59.
- Mucci, A. 1987. Influence of temperature on composition of magnesian calcite overgrowths precipitated from seawater. *Geochimica et Cosmochimica Acta*, **5**, 1977–1984.
- Muchez, Ph., Slobodnik, M., Viaene, W.A. & Keppens, E. 1995. Geochemical constraints on the origin and migration of palaeofluids at the northern margin of the Variscan foreland, southern Belgium. *Sedimentary Geology*, **96**, 191–200.
- Pili, E., Poitrasson, F. & Gratier, J.P. 2002. Carbon-oxygen isotope and trace element constraints on how fluids percolate faulted limestones from San Andreas Fault system: partitioning of fluid sources and pathways. *Chemical Geology*, **190**, 231–250.
- Pin, C. & Bassin, C. 1992. Evaluation of a strontium-specific extraction chromatographic method for isotopic analysis in geological materials. *Anal. Chim. Acta*, **269**, 249–255.
- Roca, E. 1996. La evolución geodinámica de la Cuenca Catalano-Balear y áreas adyacentes desde el Mesozoico hasta la actualidad. *Acta Geológica Hispánica*, **29**, 3–25.
- Roca, E. & Guimerà, J. 1992. The Neogene structure of the eastern Iberian margin: structural constraints on crustal evolution of the Valencia Trough (western Mediterranean). *Tectonophysics*, **203**, 203–218.
- Roca, E., Sans, M., Cabrera, L. & Marzo, M. 1999. Oligocene to Middle Miocene evolution of the central Catalan margin (northwestern Mediterranean). *Tectonophysics*, **315**, 209–233.
- Salas, R. 1987. *El Malm i el Cretaci inferior entre el Massís de Garraf i la Serra d'Espadà*. PhD thesis, University of Barcelona, Barcelona, Spain.
- Sibson, R.H. 2000. Fluid involvement in normal faulting. *Journal of Geodynamics*, **29**, 469–499.
- Steiger, R.H. & Jäger, E. 1977. Subcommittee on geochronology: convention on the use of decay constants in geo- and cosmochronology. *Earth and Planetary Science Letters*, **36**, 359–362.
- Stewart, I.S. & Hancock, P.L. 1990. Brecciation and fracturing within neotectonic normal fault zones of the Aegean region. In: Knipe, R.J. & Rutter, E.H. (eds) *Deformation Mechanisms, Rheology and Tectonics*. Geological Society, London, Special Publications, **54**, 105–112.

- Travé, A. & Calvet, F. 2001. Syn-rift geofluids in fractures related to the early-middle Miocene evolution of the Vallès-Penedès Half-graben (NE Spain). *Tectonophysics*, **336**, 101–120.
- Travé, A., Calvet, F., Soler, A. & Labaume, P. 1998. Fracturing and fluid migration during Palaeogene compression and Neogene extension in the Catalan Coastal Ranges, Spain. *Sedimentology*, **45**, 1063–1082.
- Travé, A., Labaume, P. & Vergés, J. 2007. Fluid systems in Foreland Fold-and-Thrust Belts: An overview from the Southern Pyrenees. In: Lacombe, O., Lavé, J., Roure, F. & Vergés, J. (eds) *Thrust Belts and Foreland Basins. From fold kinematics to hydrocarbon systems*. Springer Verlag, Berlin.
- Tucker, M.E. & Wright, V.P. 1990. *Carbonate Sedimentology*. Blackwell Scientific, Oxford.
- Veizer, J. & Hoefs, J. 1976. The nature of O^{18}/O^{16} and C^{13}/C^{12} secular trends in sedimentary carbonate rocks. *Geochimica et Cosmochimica Acta*, **40**, 1387–1395.
- Veizer, J., Buhl, D. & Diener, A. *et al.* 1997. Strontium isotope stratigraphy: potential resolution and event correlation. *Palaeogeography, Palaeoclimatology, Palaeoecology*, **132**, 65–77.
- Veizer, J., Ala, D. & Azmy, K. *et al.* 1999. $^{87}Sr/^{86}Sr$, $\delta^{13}C$ and $\delta^{18}O$ evolution of Phanerozoic seawater. *Chemical Geology*, **161**, 59–88.
- Verhaert, G., Muechez, P., Deppens, E. & Sintubin, M. 2009. Fluid impact and spatial and temporal evolution of normal faulting in limestones. A case study in the Burdur-Isparta Region (SW Turkey). *Geologica Belgica*, **12/3**, 59–73.
- Vidal, N., Gallart, J., Dañobeitia, J. & Díaz, J. 1995. Mapping the Moho in the Iberian Mediterranean margin by multicoverage processing and merging of wide-angle and near-vertical reflection data. In: Banda, E., Tomé, M. & Talwani, M. (eds) *Rifted Ocean Continent Boundaries*. NATO ASI Series Series C, Mathematical and Physical Sciences, 463, 291–308.
- Vilasi, N., Malandain, J. & Barrier, L. *et al.* 2009. From outcrop and petrographic studies to basin-scale fluid flow modeling: The use of the Albanian natural laboratory for carbonate reservoir characterization. *Tectonophysics*, **474**, 367–392.
- Wibberley, C., Petit, J. & Rives, T. 2007. The effect of tilting on fault propagation and network development in sandstone–shale sequences: a case study from the Lodève Basin, southern France. *Journal of the Geological Society, London*, **164**, 599–608.

Received 1 March 2011; revised typescript accepted 7 November 2011.